

A library of atomically thin metal chalcogenides

Jiadong Zhou^{1,15}, Junhao Lin^{2,15*}, Xiangwei Huang³, Yao Zhou⁴, Yu Chen⁵, Juan Xia⁵, Hong Wang¹, Yu Xie⁶, Huimei Yu⁷, Jincheng Lei⁶, Di Wu^{8,9}, Fucui Liu¹, Qundong Fu¹, Qingsheng Zeng¹, Chuang-Han Hsu^{8,9}, Changli Yang^{3,10}, Li Lu^{3,10}, Ting Yu⁵, Zexiang Shen⁵, Hsin Lin^{8,9,11}, Boris I. Yakobson⁶, Qian Liu⁴, Kazu Suenaga², Guangtong Liu^{3*} & Zheng Liu^{1,12,13,14*}

Investigations of two-dimensional transition-metal chalcogenides (TMCs) have recently revealed interesting physical phenomena, including the quantum spin Hall effect^{1,2}, valley polarization^{3,4} and two-dimensional superconductivity⁵, suggesting potential applications for functional devices^{6–10}. However, of the numerous compounds available, only a handful, such as Mo- and W-based TMCs, have been synthesized, typically via sulfurization^{11–15}, selenization^{16,17} and tellurization¹⁸ of metals and metal compounds. Many TMCs are difficult to produce because of the high melting points of their metal and metal oxide precursors. Molten-salt-assisted methods have been used to produce ceramic powders at relatively low temperature¹⁹ and this approach²⁰ was recently employed to facilitate the growth of monolayer WS₂ and WSe₂. Here we demonstrate that molten-salt-assisted chemical vapour deposition can be broadly applied for the synthesis of a wide variety of two-dimensional

(atomically thin) TMCs. We synthesized 47 compounds, including 32 binary compounds (based on the transition metals Ti, Zr, Hf, V, Nb, Ta, Mo, W, Re, Pt, Pd and Fe), 13 alloys (including 11 ternary, one quaternary and one quinary), and two heterostructured compounds. We elaborate how the salt decreases the melting point of the reactants and facilitates the formation of intermediate products, increasing the overall reaction rate. Most of the synthesized materials in our library are useful, as supported by evidence of superconductivity in our monolayer NbSe₂ and MoTe₂ samples^{21,22} and of high mobilities in MoS₂ and ReS₂. Although the quality of some of the materials still requires development, our work opens up opportunities for studying the properties and potential application of a wide variety of two-dimensional TMCs.

Figure 1 proposes a general picture for the synthesis of two-dimensional (2D) TMCs using the chemical vapour deposition method,

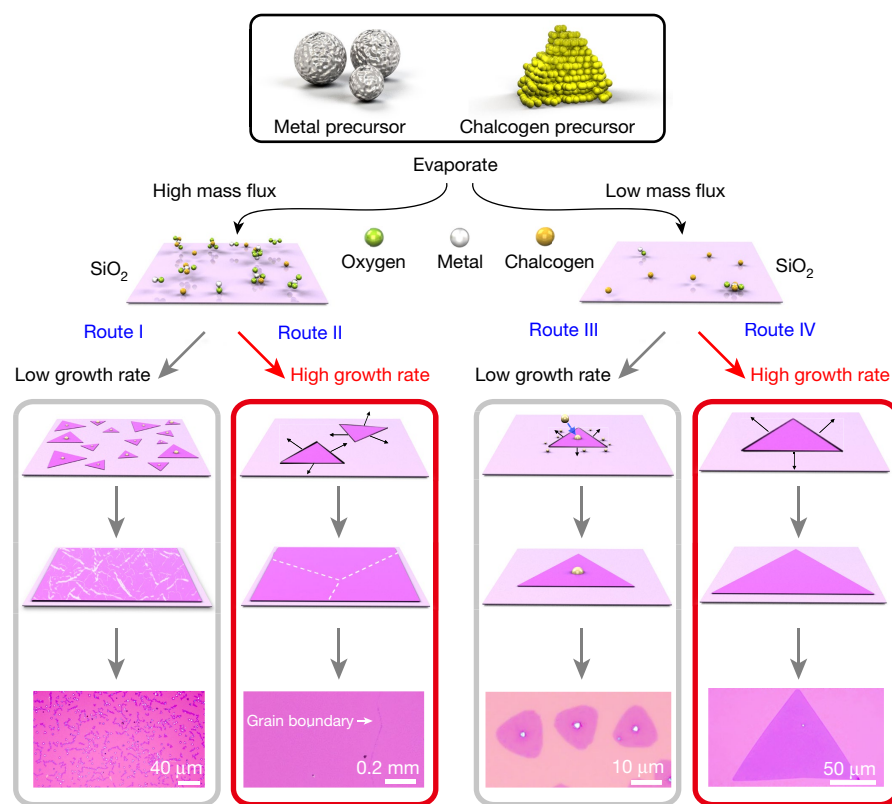


Fig. 1 | Flow chart of the general growth process for the production of TMCs by the chemical vapour deposition method. The growth of 2D TMCs can be classified into four routes based on different mass flux of metal precursor and growth rate. High mass flux of metal precursor offers the opportunity to synthesize large-scale continuous monolayer polycrystalline films with small (route I) or large (route II) domains depending on the growth rate. On the other hand, low mass flux of metal precursor results in discrete single-crystalline monolayers with different sizes. Low growth rate leads to small crystal size with atom clusters decorated in the centre and edge of the monocrystal (route III), while high growth rate gives rise to large monocrystals (route IV).

¹Center for Programmable Materials, School of Materials Science and Engineering, Nanyang Technological University, Singapore, Singapore. ²National Institute of Advanced Industrial Science and Technology (AIST), Tsukuba, Japan. ³Beijing National Laboratory for Condensed Matter Physics, Institute of Physics, Chinese Academy of Sciences, Beijing, China. ⁴The State Key Laboratory of High Performance Ceramics and Superfine Microstructure, Shanghai Institute of Ceramics, Chinese Academy of Sciences, Shanghai, China. ⁵Division of Physics and Applied Physics, School of Physical and Mathematical Sciences, Nanyang Technological University, Singapore, Singapore. ⁶Department of Materials Science and NanoEngineering and Department of Chemistry, Rice University, Houston, TX, USA. ⁷School of Materials Science and Engineering, East China University of Science and Technology, Shanghai, China. ⁸Centre for Advanced 2D Materials and Graphene Research Centre, National University of Singapore, Singapore, Singapore. ⁹Department of Physics, National University of Singapore, Singapore, Singapore. ¹⁰Collaborative Innovation Center of Quantum Matter, Beijing, China. ¹¹Institute of Physics, Academia Sinica, Taipei, Taiwan. ¹²Centre for Micro-/Nano-electronics (NOVITAS), School of Electrical and Electronic Engineering, Nanyang Technological University, Singapore, Singapore. ¹³CINTRA CNRS/NTU/THALES, UMI 3288, Research Techno Plaza, Singapore, Singapore. ¹⁴Environmental Chemistry and Materials Centre, Nanyang Environment and Water Research Institute, Singapore, Singapore. ¹⁵These authors contributed equally: Jiadong Zhou, Junhao Lin. *e-mail: lin.junhao.stem@gmail.com; gtlou@phy.ac.cn; z.liu@ntu.edu.sg

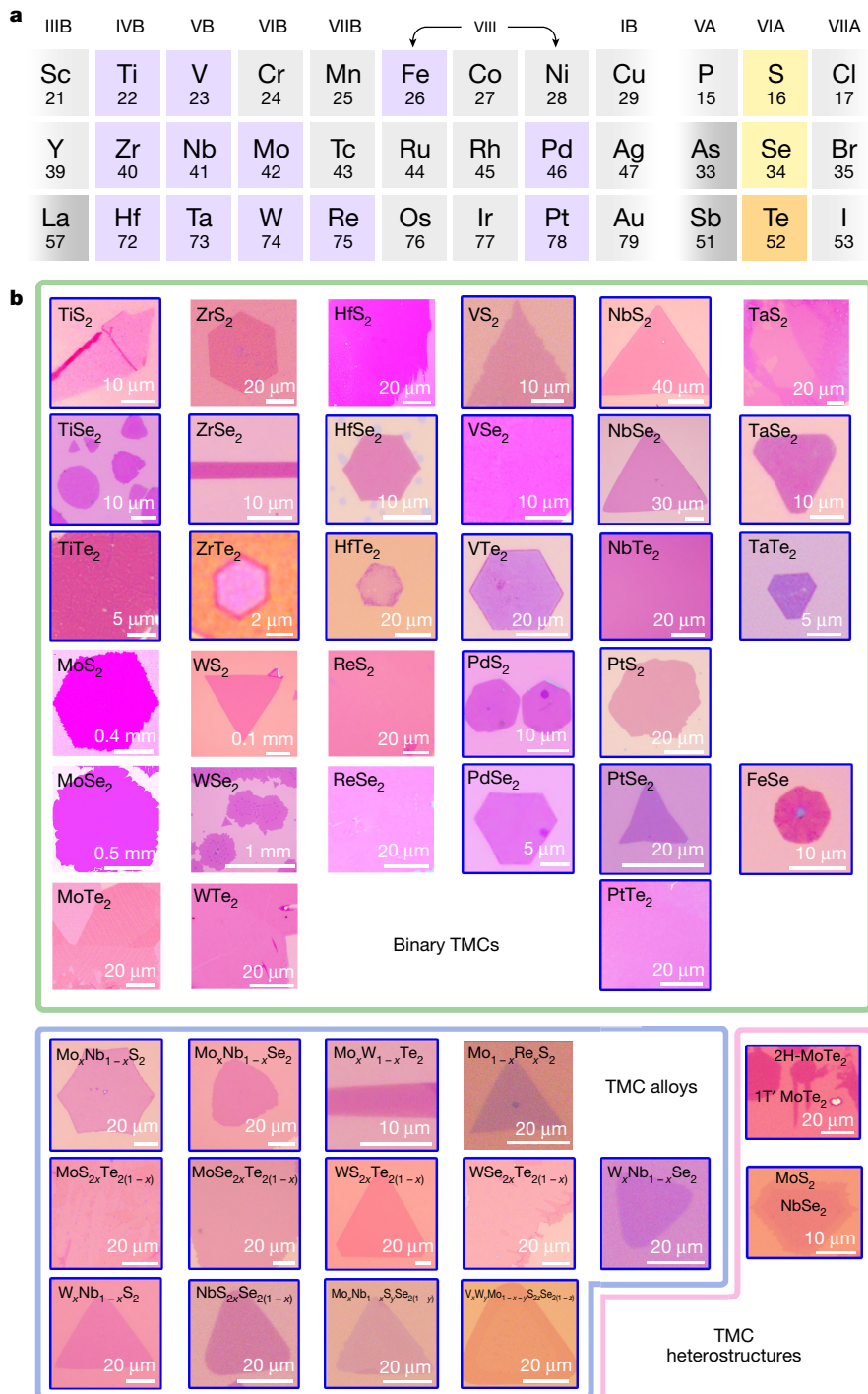


Fig. 2 | The transition metals and chalcogens used, and optical images of the resulting 47 different atomically thin TMCs and heterostructures. a, Overview of metals (highlighted in purple) and chalcogens (highlighted in yellow and orange) that can form layered sulfides, selenides and tellurides. **b**, Optical images of 47 TMCs synthesized using our method: binary 2D crystals containing Mo (MoS_2 , MoSe_2 , MoTe_2), W (WS_2 , WSe_2 , WTe_2), Re (ReS_2 , ReSe_2), Ti (TiS_2 , TiSe_2 , TiTe_2), Zr (ZrS_2 , ZrSe_2 , ZrTe_2), Hf (HfS_2 , HfSe_2 , HfTe_2), V (VS_2 , VSe_2 , VTe_2), Nb (NbS_2 , NbSe_2 , NbTe_2), Ta (TaS_2 , TaSe_2 , TaTe_2), Pt (PtS_2 , PtSe_2 ,

PtTe_2), Pd (PdS_2 , PdSe_2) or Fe (FeSe); the ternary alloys $\text{Mo}_x\text{Te}_{2-x}$, $\text{MoSe}_x\text{Te}_{2-x}$, $\text{WS}_x\text{Te}_{2-x}$, $\text{WSe}_x\text{Te}_{2-x}$, $\text{NbS}_x\text{Se}_{2-x}$, $\text{Mo}_x\text{Nb}_{1-x}\text{S}_2$, $\text{Mo}_x\text{Nb}_{1-x}\text{Se}_2$, $\text{Mo}_{1-x}\text{Re}_x\text{S}_2$, $\text{W}_x\text{Nb}_{1-x}\text{S}_2$, $\text{W}_x\text{Nb}_{1-x}\text{Se}_2$ and $\text{Mo}_x\text{W}_{1-x}\text{Te}_2$; the quaternary alloy $\text{Mo}_x\text{Nb}_{1-x}\text{S}_{2y}\text{Se}_{2(1-y)}$; the quinary alloy $\text{V}_x\text{W}_y\text{Mo}_{1-x-y}\text{S}_{2z}\text{Se}_{2(1-z)}$; and the 1 T' MoTe_2 -2 H MoTe_2 in-plane and MoS_2 - NbSe_2 vertically stacked heterostructures. TMCs that have not been previously synthesized are outlined in blue. Detailed characterizations of the as-grown 2D materials are shown in Supplementary Information.

based on the competition between the mass flux of the metal precursors and the reaction rate of the domains. The mass flux determines the amount of metal precursors involved in the formation of the nucleus and the growth of domains, whereas the growth rate dominates the grain size of the as-grown films. At high mass flux, low growth rate results in a monolayer polycrystalline film (route I) with small grains,

and high growth rate tends to form continuous monolayer films with large grains of up to millimetres in size (route II)²³. On the other hand, at low mass flux, low growth rate promotes the formation of small flakes. Tiny nuclei are often observed at the centre of the flakes²⁴, suggesting that the extra adatoms or atom clusters will consistently attach to an existing nucleus or to the edge during growth (route III). A high

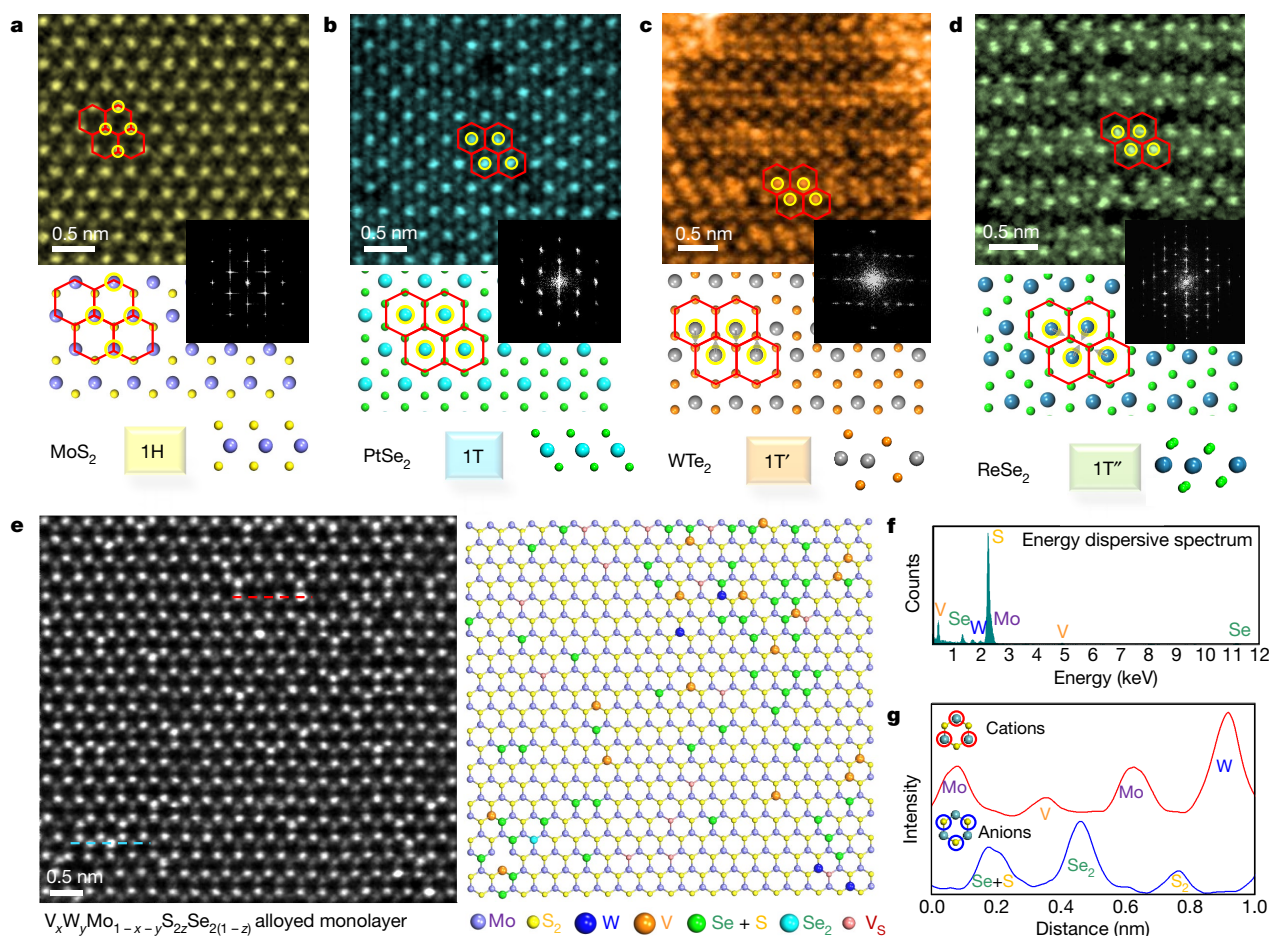


Fig. 3 | Atomic-resolution STEM images of representative monolayer materials in different phases. a–d, MoS₂ in the 1H phase (a), PtSe₂ in the 1T phase (b), WTe₂ in the 1T' phase (c) and ReSe₂ in the 1T'' phase (d), with their corresponding fast Fourier transform patterns and atomic structural models. e, STEM image (left) of the quinary monolayer alloy

$V_xW_yMo_{1-x-y}S_{2z}Se_{2(1-z)}$, with the corresponding atomic model from atom-by-atom intensity mapping (right). f, EDS spectra of the alloyed monolayer, confirming its chemical composition. g, Line intensity profiles along the highlighted red (cation) and blue (anion) dashed lines in e, indicating the different intensity of each chemical species.

reaction rate preferentially produces a monolayer of individual large 2D single crystals (route IV)²⁵.

Unfortunately, many TMCs, such as those based on Nb, Pt and Ti, are very difficult to produce because their metal or metal oxide precursors have high melting points and low vapour pressure, which leads to very low mass flux and limits the reaction. Molten salts can increase mass flux by reducing the melting points of the metal precursors and forming oxychlorides via reaction with some metal oxides, thus increasing the rate of the reaction. Using this method, we have synthesized a library of 2D TMCs (shown in Fig. 2).

Figure 2a shows a schematic of the periodic table, highlighting the chemical combination of all the 2D TMC atomic layers produced, formed between 12 transition metals (purple) and three chalcogens (yellow). Synthetic recipes and reaction conditions are illustrated in Methods and are summarized in Supplementary Fig. 1 and Supplementary Table 1. Figure 2b shows optical images of 47 2D TMC compounds with morphologies of triangles, hexagons, ribbons and films, including 32 binary crystals from group IVB (Ti, Zr and Hf) to group VIII (Pd and Pt), 13 alloyed TMCs (containing ternary, quaternary and even quinary compounds), which are important for universal bandgap engineering and heterogeneous catalysis^{26–29}, and two heterostructure TMCs (vertically stacked MoS₂–NbSe₂ and in-plane 1T' MoTe₂–2H MoTe₂). The 2D TMCs that had not previously been synthesized are outlined in blue. Detailed characterizations of all 2D TMCs and heterostructures are presented in Supplementary Figs. 2–11.

The atomic structures and chemical compositions of the as-synthesized 2D crystals and compounds are further revealed by atom-resolved scanning transmission electron microscopy (STEM)

imaging, energy-dispersive X-ray spectroscopy (EDS) and electron energy loss spectroscopy (EELS). The atomic structures of most 2D crystals can be classified into four types: (1) the trigonal prismatic 1H phase; (2) the undistorted 1T phase with the metal atom located at the centre of an octahedral unit; (3) the one-dimensional distorted 1T phase (called the 1T' phase), in which pairs of metal atoms move closer to each other perpendicularly, resulting in a quasi-one-dimensional chain-like structure consisting of distorted octahedral units; and (4) the two-dimensional distorted 1T phase (called the 1T'' phase), in which four nearby metal atoms move closer to each other to form a new unit cell, producing repeatable diamond-like patterns. The structural phase of each synthesized material can be determined by the Z-contrast STEM image. Figure 3a–d shows the representative materials for each phase with the corresponding atomic structural models; these materials are monolayer MoS₂, PtSe₂, WTe₂ and ReSe₂ for the 1H, 1T, 1T' and 1T'' phases, respectively. The patterns obtained by fast Fourier transform further indicate that the 1H and 1T phases maintain a hexagonal unit cell, whereas the 1T' phase forms a rectangular unit cell owing to one-dimensional metal-pair distortion and the 1T'' phase changes to a much larger hexagonal cell owing to the aggregation of four metal atoms into a new unit cell. A summary of different phases for each as-synthesized 2D material that has been examined is shown in Supplementary Fig. 12. Details of the atomic structure, EDS and EELS characterizations for each 2D crystal are given in Supplementary Figs. 13–27.

A STEM image of a quinary $V_xW_yMo_{1-x-y}S_{2z}Se_{2(1-z)}$ monolayer alloy is shown in Fig. 3e, where the chemical composition is verified by the EDS spectrum (Fig. 3f). The corresponding optical image

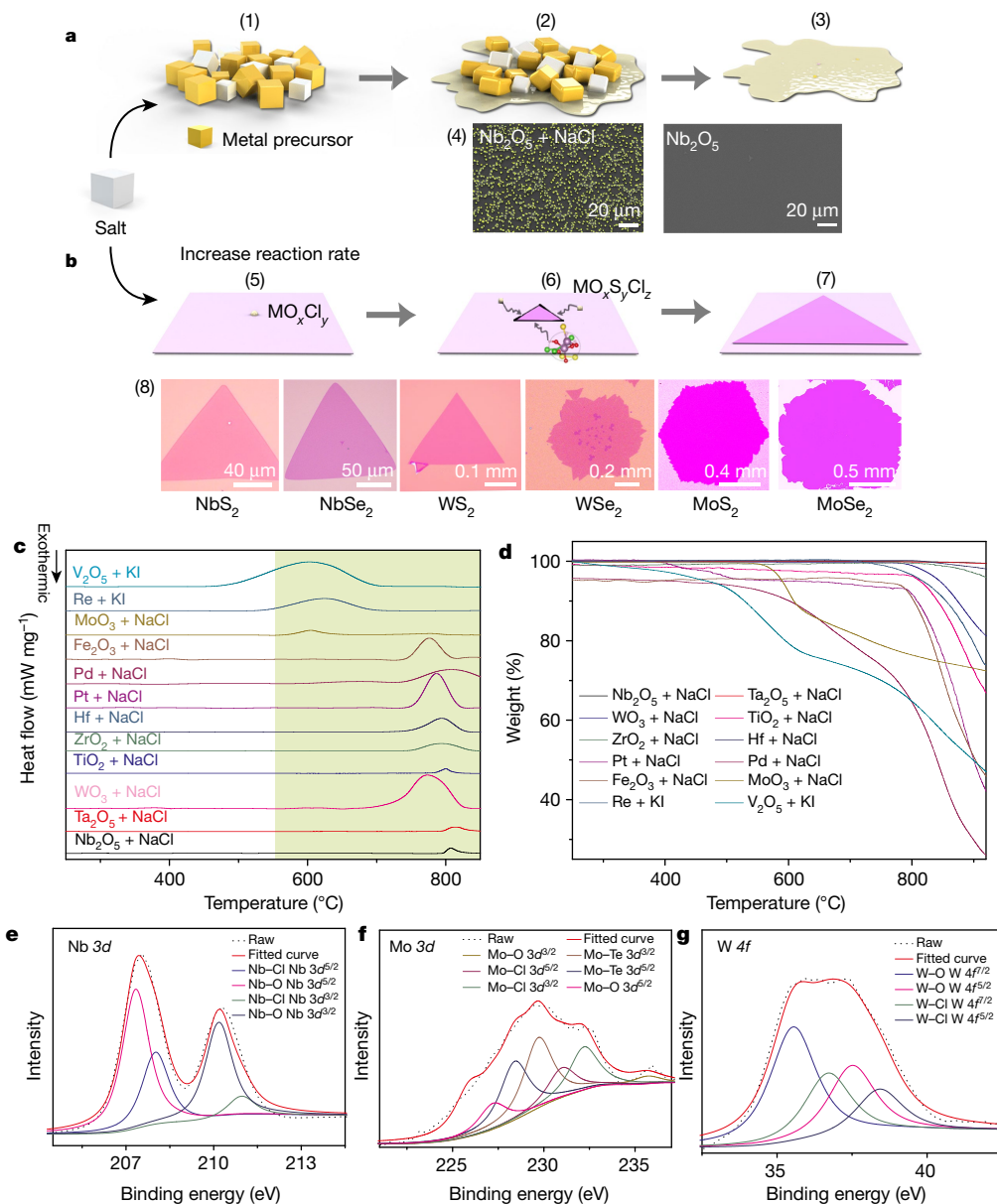


Fig. 4 | Reaction mechanism. **a, b**, Schematics of the reactions. Metal oxychlorides are formed, and these promote the reactions. Chalcogens are not shown here. (1)–(3) The proposed process of the added salt decreasing the melting point of the precursors. (4) SEM images of the Nb nucleus with (left) and without (right) added salt. **b**, (5)–(7) The growth process of the 2D atomic layer, with intermediate products. (8) Different single-crystalline monolayers with large size of monolayer and a growth time of less than 3 min. **c, d**, The TG-DSC curve of salts mixed with the metal sources. The melting points of the systems after adding salt are all

within the highlighted windows from 600 °C to 850 °C. **e–g**, XPS spectra revealing the existence of Cl bonds to other elements, resulting from the intermediate products during the synthesis of Nb-, Mo- and W-based 2D crystals. XPS spectra of Nb 3d, Mo 3d and W 4f are shown in **e, f** and **g**, respectively. Nb 3d^{3/2} and 3d^{5/2}, Mo 3d^{3/2} and 3d^{5/2} and W 4f^{5/2} and 4f^{7/2} are the core level energy states of Nb, Mo and W, respectively, all of which are well fitted with Gaussian peaks at energies indicating the bonding to Cl.

and Raman spectrum are shown in Supplementary Fig. 9. Different chemical species give rise to the distinct atomic contrast in the image. Combined with the intensity histogram analysis of the cation and anion sites (Supplementary Fig. 28), each atomic column can be directly associated with their chemical identities using the image contrast, as shown by the representative line intensity profile in Fig. 3g. The atom-by-atom mapping further confirms the successful synthesis of a quinary alloyed monolayer. We also observe superconductivity in monolayer NbSe₂ and MoTe₂ (Supplementary Figs. 29–31)^{21,22}, which is the realization of superconductivity in non-ultrahigh-vacuum-grown monolayer materials. Combined with the high mobility of monolayer MoS₂ and ReS₂ (Supplementary Figs. 32 and 33), these results indicate the high quality of the as-prepared 2D TMCs. We note that most of the as-synthesized materials show well controlled thickness and useful

attributes, but some, such as ZrTe₂, TiTe₂, HfTe₂ and the Pd-based ones, need to be further improved.

The growing mechanism of the salt-assisted chemical vapour deposition method is discussed in Fig. 4 and detailed in Supplementary Figs. 34–53). Figure 4a illustrates that salt can reduce the melting points of metal precursors, and thus make the reaction possible (see also Supplementary Fig. 35) to grow 2D TMCs. As an example, a comparison of the observed Nb nucleus with and without salt added is shown in Fig. 4a, indicating a high mass flux of the metal precursors promoted by the salt. In addition to decreases of the melting point, Fig. 4b shows that some metal oxides can react with salt to form metal oxychlorides, which evaporate at an appropriate temperature and facilitate the growth of the 2D TMCs. We obtained the melting points of the precursors for all binary 2D systems using thermogravimetry and

differential scanning calorimetry (TG-DSC) measurements. They all fell within the temperature window from 600 °C to 850 °C, as shown in Fig. 4c, which matches the temperature range in which the resulting materials grow. This is further supported by the thermogravimetry versus time curves in Fig. 4d. During the growth, coarsening forms a stable nucleus (Supplementary Fig. 38), then adatoms and atom clusters of chalcogen and metal attach to the edges of as-grown 2D monolayers and grow quickly owing to their high mobility (Supplementary Figs. 47 and 48). This growth process is supported by experimental evidence (Supplementary Figs. 49–51), and also previous reports³⁰ on MoS₂. This helps to produce millimetre-sized single-crystal 2D TMCs, such as the W-, Nb- and Mo-based TMCs (Fig. 4b). Notably, the growth time in our experiment is as short as 3 min and the growth rate is up to 8 μm s⁻¹ (Supplementary Figs. 39 and 40), owing to the high chemical activities of oxychloride during the reaction. To confirm the existence of metal oxychloride, the intermediate products are collected and analysed by X-ray photoelectron spectroscopy (XPS) during the synthesis of monolayer NbX₂, MoX₂ and WX₂ (X = S, Se, Te). The signals from M–Cl and M–O (M = W, Nb, Mo) bonds in Nb 3d, Mo 3d and W 4f (Fig. 4e–g) confirm the existence of the oxychloride compounds^{31–33} NbO_xCl_y, MoO_xCl_y and WO_xCl_y (see also Supplementary Figs. 52 and 53). Moreover, the formation of metal oxychloride is also corroborated by ab initio molecular dynamics simulations (Supplementary Figs. 36 and 37). The density functional theory calculations show that it is energetically more favourable to sulfurize metal oxychlorides than metal oxides.

In conclusion, we have demonstrated a universal salt-assisted chemical vapour deposition method for producing a 2D TMC library consisting of 47 compounds and heterostructures. Our work provides a swift way to produce good-quality 2D TMCs. Our understanding of the growth mechanism is greatly improved, suggesting ways to explore the extraordinary physical characteristics of these materials and their nanodevice applications.

Online content

Any Methods, including any statements of data availability and Nature Research reporting summaries, along with any additional references and Source Data files, are available in the online version of the paper at <https://doi.org/10.1038/s41586-018-0008-3>.

Received: 31 December 2016; Accepted: 26 January 2018;

Published online 18 April 2018.

- Zhang, Y. B., Tan, Y. W., Stormer, H. L. & Kim, P. Experimental observation of the quantum Hall effect and Berry's phase in graphene. *Nature* **438**, 201–204 (2005).
- Qian, X. F., Liu, J. W., Fu, L. & Li, J. Quantum spin Hall effect in two-dimensional transition metal dichalcogenides. *Science* **346**, 1344–1347 (2014).
- Xiao, D., Liu, G. B., Feng, W. X., Xu, X. D. & Yao, W. Coupled spin and valley physics in monolayers of MoS₂ and other group-VI dichalcogenides. *Phys. Rev. Lett.* **108**, 196802 (2012).
- Zeng, H. L., Dai, J. F., Yao, W., Xiao, D. & Cui, X. D. Valley polarization in MoS₂ monolayers by optical pumping. *Nat. Nanotechnol.* **7**, 490–493 (2012).
- Saito, Y., Nojima, T. & Iwasa, Y. Highly crystalline 2D superconductors. *Nat. Rev. Mater.* **2**, 16094 (2017).
- Novoselov, K. S. et al. Electric field effect in atomically thin carbon films. *Science* **306**, 666–669 (2004).
- Radisavljevic, B. & Kis, A. Mobility engineering and a metal-insulator transition in monolayer MoS₂. *Nat. Mater.* **12**, 815–820 (2013).
- Wang, Q. H., Kalantar-Zadeh, K., Kis, A., Coleman, J. N. & Strano, M. S. Electronics and optoelectronics of two-dimensional transition metal dichalcogenides. *Nat. Nanotechnol.* **7**, 699–712 (2012).
- Roy, K. et al. Graphene-MoS₂ hybrid structures for multifunctional photoresponsive memory devices. *Nat. Nanotechnol.* **8**, 826–830 (2013).
- Lopez-Sanchez, O., Lembke, D., Kayci, M., Radenovic, A. & Kis, A. Ultrasensitive photodetectors based on monolayer MoS₂. *Nat. Nanotechnol.* **8**, 497–501 (2013).
- Zhan, Y. J., Liu, Z., Najmaei, S., Ajayan, P. M. & Lou, J. Large-area vapor-phase growth and characterization of MoS₂ atomic layers on a SiO₂ substrate. *Small* **8**, 966–971 (2012).
- van der Zande, A. M. et al. Grains and grain boundaries in highly crystalline monolayer molybdenum disulphide. *Nat. Mater.* **12**, 554–561 (2013).
- Lee, Y. H. et al. Synthesis of large-area MoS₂ atomic layers with chemical vapor deposition. *Adv. Mater.* **24**, 2320–2325 (2012).
- Lin, Y. C. et al. Wafer-scale MoS₂ thin layers prepared by MoO₃ sulfurization. *Nanoscale* **4**, 6637–6641 (2012).
- Elias, A. L. et al. Controlled synthesis and transfer of large-area WS₂ sheets: from single layer to few layers. *ACS Nano* **7**, 5235–5242 (2013).
- Lu, X. et al. Large-area synthesis of monolayer and few-layer MoSe₂ films on SiO₂ substrates. *Nano Lett.* **14**, 2419–2425 (2014).
- Huang, J. K. et al. Large-area synthesis of highly crystalline WSe₂ monolayers and device applications. *ACS Nano* **8**, 923–930 (2014).
- Park, J. C. et al. Phase-engineered synthesis of centimeter-scale 1T'- and 2H-molybdenum ditelluride thin films. *ACS Nano* **9**, 6548–6554 (2015).
- Kimura, T. in *Advances in Ceramics—Synthesis and Characterization Processing and Specific Applications* (ed. Sikalidis, C.) Ch. 2 (InTech, London, 2011).
- Li, S. S. et al. Halide-assisted atmospheric pressure growth of large WSe₂ and WS₂ monolayer crystals. *Appl. Mater. Today* **1**, 60–66 (2015).
- Xi, X. X. et al. Ising pairing in superconducting NbSe₂ atomic layers. *Nat. Phys.* **12**, 139–143 (2016).
- Xi, X. X. et al. Strongly enhanced charge-density-wave order in monolayer NbSe₂. *Nat. Nanotechnol.* **10**, 765–769 (2015).
- Dumcenco, D. et al. Large-area epitaxial monolayer MoS₂. *ACS Nano* **9**, 4611–4620 (2015).
- Li, B. et al. Solid-vapor reaction growth of transition-metal dichalcogenide monolayers. *Angew. Chem. Int. Ed.* **55**, 10656–10661 (2016).
- Gong, Y. J. et al. Synthesis of millimeter-scale transition metal dichalcogenides single crystals. *Adv. Funct. Mater.* **26**, 2009–2015 (2016).
- Chen, Y. F. et al. Tunable band gap photoluminescence from atomically thin transition-metal dichalcogenide alloys. *ACS Nano* **7**, 4610–4616 (2013).
- Gong, Y. J. et al. Band gap engineering and layer-by-layer mapping of selenium-doped molybdenum disulfide. *Nano Lett.* **14**, 442–449 (2014).
- Lin, Z. et al. Facile synthesis of MoS₂ and Mo_{1-x}W_x triangular monolayers. *APL Mater.* **2**, 092514 (2014).
- Azizi, A. et al. Spontaneous formation of atomically thin stripes in transition metal dichalcogenide monolayers. *Nano Lett.* **16**, 6982–6987 (2016).
- Fei, L. et al. Direct TEM observations of growth mechanisms of two-dimensional MoS₂ flakes. *Nat. Commun.* **7**, 12206 (2016).
- Wu, H.-M. & Chen, S.-A. Dopant-polymer interaction: WCl₆ doped polyacetylene. *Synth. Met.* **20**, 169–183 (1987).
- Alov, N. V. XPS study of MoO₃ and WO₃ oxide surface modification by low-energy Ar⁺ ion bombardment. *Phys. Stat. Solidi C* **12**, 263–266 (2015).
- McGuire, G. E., Schweitz, G. K. & Carlson, T. A. Study of core electron binding-energies in some group IIIA, VB, and VIB compounds. *Inorg. Chem.* **12**, 2450–2453 (1973).

Acknowledgements This work was supported by the Singapore National Research Foundation under NRF award number NRF-NRFF2013-08, Tier 2 MOE2016-T2-2-153, MOE2016-T2-1-131, MOE2015-T2-2-007, Tier 1 RG164/15, Tier 1 RG4/17, CoE Industry Collaboration Grant WINTECH-NTU and the A*Star QTE programme. T.Y. acknowledges MOE Tier 1 RG100/15. J.L. and K.S. acknowledge the financial support of JST-ACCEL and JSPS KAKENHI (JP16H06333 and P16382). The work in SICCCAS was supported by the National Key Research and Development Program of China (2016YFB0700204) and the National Natural Science Foundation of China (51502327). The work at IOP was supported by the Ministry of Science and Technology of China (grant numbers 2014CB920904, 2015CB921101 and 2016YFA0300600), the National Natural Science Foundation of China (grant numbers 11174340, 912212012, 11527806 and 91421303) and the Chinese Academy of Sciences (grant numbers XDB07010100). H.L. acknowledges the Singapore National Research Foundation for support under NRF award number NRF-NRFF2013-03. The work at Rice was supported by the US Department of Energy (DE-SC0012547) and by the R. Welch Foundation (C-1590).

Reviewer information Nature thanks D. Akinwande, M. Terrones and the other anonymous reviewer(s) for their contribution to the peer review of this work.

Author contributions J.Z. and Z.L. designed the experiments. J.Z. grew all materials except TiSe₂, NbSe₂ and TaSe₂. H.W. grew TiSe₂, NbSe₂ and TaSe₂. Y.C., J.X., J.Z., T.Y. and Z.S. carried out Raman characterizations. J.L. and K.S. performed the STEM characterizations of all samples and analysis. J.Z. performed the AFM characterization of the samples. Y.Z., H.Y. and Q.L. performed the TG-DSC and XPS testing. Y.X., J.L. and B.I.Y. worked on ab initio reaction dynamics. C.-H.H., D.W. and H.L. performed electronic structure calculations. X.H., Q.Z., F.L. and Q.F. fabricated the devices. X.H., G.L., C.Y. and L.L. measured the superconductivity in MoTe₂ and NbSe₂. J.Z., J.L. and Z.L. wrote the paper. All authors discussed and commented on the manuscript.

Competing interests The authors declare no competing interests.

Additional information

Supplementary information is available for this paper at <https://doi.org/10.1038/s41586-018-0008-3>.

Reprints and permissions information is available at <http://www.nature.com/reprints>.

Correspondence and requests for materials should be addressed to J.L. or G.L. or Z.L.

Publisher's note: Springer Nature remains neutral with regard to jurisdictional claims in published maps and institutional affiliations.

METHODS

The 2D compounds and heterostructures were synthesized in a quartz tube with diameter 1 inch. The length of the furnace is about 36 cm. The system of the reaction is shown in Supplementary Fig. 32. A mixture of H_2/Ar was used as the carrier gas. Specifically, an aluminium oxide boat with volume about $8\text{ cm} \times 1.1\text{ cm} \times 1.2\text{ cm}$ containing precursor powder was placed in the centre of the tube. The precursor powder and the salt were mixed together first. The Si substrate with a 285 nm top layer of SiO_2 was placed on the aluminium oxide boat with the polished surface down; the distance between the sources and substrate ranges from 0.2 cm to 1.2 cm. Another aluminium boat containing S or Se or Te powder was placed on the upstream (upwind) of the tube furnace at 200 °C, 300 °C and 450 °C, respectively. The distance between the S or Se or Te boat and the precursor boat is about 18 cm, 16 cm and 15 cm, respectively. The heating rate of all reactions is 50 °C min^{-1} . All the reactions were carried out at atmospheric pressure. The temperature was cooled down to room temperature naturally. All reaction materials were bought from Alfa Aesar with purity more than 99%.

MoS₂. A powder mixture of 0.5 mg NaCl and 3 mg MoO₃ in an aluminium oxide boat was placed in the centre of the quartz tube. The furnace was heated to the growing temperature (600–800 °C) with a ramp rate of 50 °C min^{-1} . The growth time is 3–5 min. Ar (or Ar/H_2) with a flow rate of 80 (or 80/5) sccm (cubic centimetres per minute) was used as the carrier gas.

MoSe₂. The synthesis recipe for MoSe₂ is similar to that of MoS₂. The growth temperature was about 700–800 °C, and Ar/H_2 with a flow rate of 80/5 sccm was used as the carrier gas.

MoTe₂. A powder mixture of 4 mg NaCl and 14 mg MoO₃ in the aluminium oxide boat was placed in the centre of the quartz tube. The furnace was heated to the growth temperature (600–800 °C) with a ramp rate of 50 °C min^{-1} and held for 3 min before cooling down to room temperature naturally. Ar/H_2 with a flow rate of 80/20 sccm was used as the carrier gas.

WS₂. Using our method, large-size and monolayered WS₂ single crystals can be prepared at a relatively low temperature of about 750–850 °C. An aluminium oxide boat containing 6 mg NaCl and 30 mg WO₃ was placed in the centre of the quartz tube. The furnace was heated with a ramp rate of 50 °C min^{-1} to the growth temperature (750–850 °C) and held for 3 min. Ar/H_2 at flow rate 80/10 sccm was used as the carrier gas.

WSe₂. The growth process of WSe₂ was similar to that of WS₂. The size of the monolayered WSe₂ single crystal can reach 1 mm.

WTe₂. A powder mixture of 15 mg NaCl and 60 mg WO₃ in the boat was placed in the centre of the quartz tube. The furnace was heated with a ramp rate of 50 °C min^{-1} to the growth temperature (750–850 °C) and held at this temperature for 3 min before cooling down to room temperature naturally. Ar/H_2 with a flow rate of 80/20 sccm was used as the carrier gas.

TiS₂. A powder mixture of 3 mg NaCl and 10 mg TiO₂ in the aluminium oxide boat was placed in the centre of the quartz tube. The furnace was heated with a ramp rate of 50 °C min^{-1} to the growth temperature (750–810 °C) and held at this temperature for 8–15 min before cooled down to room temperature naturally. Ar/H_2 with a flow rate of 80/20 sccm was used as the carrier gas. Using our method, monolayer TiS₂ with a size up to 50 μm was obtained.

TiSe₂. The parameters for the growth of TiSe₂ are similar to those of TiS₂ but replacing S with Se. Ar/H_2 with a flow rate of 100/20 sccm was used as the carrier gas.

TiTe₂. A powder mixture of 3 mg NaCl and 10 mg TiO₂ (note that Ti powder can be used) in the aluminium oxide boat was placed in the centre of the quartz tube. The furnace was heated with a ramp rate of 50 °C min^{-1} to the growth temperature (800–850 °C) and held at this temperature for 10–15 min before cooling down to room temperature naturally. Ar/H_2 with a flow rate of 110/20 sccm was used as the carrier gas.

ZrS₂. The synthesis procedures are as follows. A powder mixture of 3 mg NaCl and 10 mg ZrO₂ (note that Zr powder can be used) in the aluminium oxide boat was placed in the centre of the quartz tube. The furnace was heated with a ramp rate of 50 °C min^{-1} to the growth temperature (750–800 °C) and held at this temperature for 10–15 min before cooling down to room temperature naturally. Ar/H_2 with a flow rate of 100/20 sccm was used as the carrier gas.

ZrSe₂. Similar to the synthesis of ZrS₂ but replacing S with Se powder and raising the growth temperature to 750–830 °C.

ZrTe₂. Similar to the synthesis of ZrS₂ but replacing S with Te powder and raising the growth temperature to 800–850 °C.

HfS₂. The synthetic procedures are as follows. A powder mixture of 3 mg NaCl and 5 mg Hf in the aluminium oxide boat was placed in the centre of the quartz tube. Another aluminium oxide boat containing S powder was placed in the upstream. The furnace was heated with a ramp rate of 50 °C min^{-1} to the growth temperature (800–850 °C) and held at this temperature for 10–15 min before cooling down to room temperature naturally. Ar with a flow rate of 120 sccm was used as the carrier gas.

HfSe₂. Similar to the synthesis of HfS₂ but replacing S with Se powder and raising the growth temperature to 750–850 °C. Ar/H_2 with a flow rate of 120/20 sccm was used as the carrier gas.

HfTe₂. Similar to the synthesis of HfS₂ but replacing S with Te powder and raising the growth temperature to 800–850 °C. Ar/H_2 with a flow rate of 120/20 sccm was used as the carrier gas.

VS₂, VSe₂ and VTe₂. A powder mixture of 1 mg KI and 3 mg V₂O₅ in the aluminium oxide boat was placed in the centre of the quartz tube. Another aluminium oxide boat containing S/Se/Te powder was placed in the upstream. The furnace was heated with a ramp rate of 50 °C min^{-1} to the growth temperature (680–750 °C) and held at this temperature for 10–15 min before cooling down to room temperature naturally. Ar/H_2 with a flow rate of 80/16 sccm was used as the carrier gas.

NbS₂, NbSe₂ and NbTe₂. A mixed powder of 2 mg NaCl and 10 mg Nb₂O₅ in the aluminium oxide boat was placed in the centre of the quartz tube. Another aluminium oxide boat containing S/Se/Te powder was placed in the upstream. The furnace was heated with a ramp rate of 50 °C min^{-1} to the growth temperatures (750–850 °C) and held at this temperature for 3–5 min before cooled down to room temperature naturally. Ar/H_2 with a flow rate of 80/16 sccm was used as carrier gas.

TaS₂, TaSe₂ and TaTe₂. A mixed powder of 5 mg NaCl and 30 mg Ta₂O₅ in the aluminium oxide boat was placed in the centre of the quartz tube. Another aluminium oxide boat containing S/Se/Te powder was placed in the upstream. The furnace was heated with a ramp rate of 50 °C min^{-1} to the growth temperature (800–850 °C) and held at this temperature for 10–20 min before cooling down to room temperature naturally. The Ar/H_2 with a flow rate of 100/18 sccm was used as carrier gas.

ReS₂. A mixed powder of 1 mg KI and 5 mg Re in the aluminium oxide boat was placed in the centre of the quartz tube. The furnace was heated with a ramp rate of 50 °C min^{-1} to the growth temperature (650–750 °C) and held for 5–10 min before cooling down to room temperature naturally. Ar with a flow rate of 60 sccm was used as the carrier gas.

ReSe₂. Although the synthesis of ReS₂ has been reported, monolayer ReSe₂ has not been synthesized successfully. Here, the preparation method of ReSe₂ is similar to the synthesis of ReS₂. Se powder was used as the Se source and the reaction temperature was fixed at 700–780 °C. Ar/H_2 with a flow rate of 80/10 sccm was used as the carrier gas.

FeSe. A mixed powder of 2 mg NaCl and 10 mg Fe₂O₃ (or FeCl₂) in the aluminium oxide boat was placed in the centre of the quartz tube. Another aluminium oxide boat containing Se powder was placed in the upstream. The furnace was heated with a ramp rate of 50 °C min^{-1} to the growth temperature (750–850 °C) and held at this temperature for 10–20 min before cooling down to room temperature naturally. Ar/H_2 with a flow rate of 100/18 sccm was used as the carrier gas.

PtS₂, PtSe₂, PtTe₂, PdS₂ and PdSe₂. A mixture of 1 mg NaCl and 10 mg M (using Pt, Pd nanoparticles or PtCl₂, PdCl₂ powder) in the aluminium oxide boat was placed in the centre of the quartz tube. Another aluminium oxide boat containing S/Se/Te powder was placed in the upstream. The furnace was heated with a ramp rate of 50 °C min^{-1} to the growth temperature (800–850 °C) and held at this temperature for 10–20 min before cooling down to room temperature naturally. Ar/H_2 with a flow rate of 100/20 sccm was used as the carrier gas.

MoS_{2-x}Te_{2(1-x)}. A powder mixture of 2 mg NaCl and 10 mg MoO₃ in the aluminium oxide boat was placed in the centre of the tube. Another aluminium oxide boat containing a powder mixture of S and Te was placed in the upstream. The furnace was heated with a ramp rate of 50 °C min^{-1} to the growth temperature 700–800 °C and held at this temperature for 10–20 min before cooling down to room temperature naturally. Ar/H_2 with a flow rate of 100/5 sccm was used as the carrier gas.

MoSe_{2-x}Te_{2(1-x)}. Similar to the synthesis of MoS_{2-x}Te_{2(1-x)} except for using a powder mixture of Se and Te as precursor.

WS_{2-x}Te_{2(1-x)}. A powder mixture of 3 mg NaCl and 15 mg WO₃ in the aluminium oxide boat was placed in the centre of the quartz tube. Another aluminium oxide boat containing a powder mixture of S and Te was placed in the upstream. The furnace was heated with a ramp rate of 50 °C min^{-1} to the growth temperature (750–850 °C) and held at this temperature for 10–20 min before cooling down to room temperature naturally. Ar/H_2 with a flow rate of 100/5 sccm was used as the carrier gas.

WSe_{2-x}Te_{2(1-x)}. Similar to the synthesis of WS_{2-x}Te_{2(1-x)} except for using a powder mixture of Se and Te as precursor.

NbS_{2-x}Se_{2(1-x)}. A powder mixture of 2 mg NaCl and 10 mg Nb₂O₅ in the aluminium oxide boat was placed in the centre of the tube. The furnace was heated with a ramp rate of 50 °C min^{-1} to the growth temperature (760–840 °C) and held at this temperature for 10–20 min before cooling down to room temperature naturally. Ar/H_2 with a flow rate of 100/15 sccm was used as the carrier gas.

Mo_{1-x}Nb_xSe₂. A powder mixture of 2 mg NaCl and 10 mg of Nb₂O₅:MoO₃ = 1:1 in the aluminium oxide boat was placed in the centre of the quartz tube. Another aluminium oxide boat containing Se powder was placed in the upstream. The furnace was heated with a ramp rate of 50 °C min^{-1} to the growth temperature (760–840 °C) and held at this temperature for 10–20 min followed by cooling down

to room temperature naturally. Ar/H₂ with a flow rate of 100/15 sccm was used as the carrier gas.

Mo_{1-x}Re_xS₂. A powder mixture of 2 mg NaCl and 10 mg of Re:MoO₃ = 1:1 in the aluminium oxide boat was placed in the centre of the quartz tube. The furnace was heated with a ramp rate of 50 °C min⁻¹ to the growth temperature (700–800 °C) and held at this temperature for 10–20 min before cooling down to room temperature naturally. Ar/H₂ with a flow rate of 80/5 sccm was used as the carrier gas.

W_{1-x}Nb_xS₂. A powder mixture of 2 mg NaCl and 15 mg of Nb₂O₅:WO₃ = 1:1 in the aluminium oxide boat was placed in the centre of the quartz tube. The furnace was heated with a ramp rate of 50 °C min⁻¹ to the growth temperature (750–840 °C) and held at this temperature for 10–20 min before cooling down to room temperature naturally. Ar/H₂ with a flow rate of 100/15 sccm was used as the carrier gas.

W_{1-x}Nb_xSe₂. A powder mixture of 2 mg NaCl and 15 mg of Nb₂O₅:WO₃ = 1:1 in the aluminium oxide boat was placed in the centre of the quartz tube. The furnace was heated with a ramp rate of 50 °C min⁻¹ to the growth temperature (750–840 °C) and held at this temperature for 10–20 min before cooling down to room temperature naturally. Ar/H₂ with a flow rate of 100/15 sccm was used as the carrier gas.

Mo_xNb_{1-x}S₂. A powder mixture of 2 mg NaCl and 10 mg of Nb₂O₅:MoO₃ = 1:1 in the aluminium oxide boat was placed in the centre of the quartz tube. The furnace was heated with a ramp rate of 50 °C min⁻¹ to the growth temperature (760–840 °C) and held at this temperature for 10–20 min before cooling down to room temperature naturally. Ar/H₂ with a flow rate of 100/15 sccm was used as the carrier gas.

Mo_xW_{1-x}Te₂. A powder mixture of 2 mg NaCl and 10 mg of WO₃:MoO₃ = 1:1 in the aluminium oxide boat was placed in the centre of the quartz tube. The furnace was heated with a ramp rate of 50 °C min⁻¹ to the growth temperature (760–840 °C) and held at this temperature for 5–10 min before cooling down to room temperature naturally. Ar/H₂ with a flow rate of 100/15 sccm was used as the carrier gas.

Mo_xNb_{1-x}S_{2y}Se_{2(1-y)}. A powder mixture of 2 mg NaCl and 10 mg of Nb₂O₅:MoO₃ = 1:1 in the aluminium oxide boat was placed in the centre of the quartz tube. Another aluminium oxide boat containing S and Se powder was placed in the upstream. The furnace was heated with a ramp rate of 50 °C min⁻¹ to the growth temperature (760–840 °C) and held at this temperature for 10–20 min before cooling down to room temperature naturally. Ar/H₂ with a flow rate of 100/15 sccm was used as the carrier gas.

V_xW_yMo_{1-x-y}S_{2z}Se_{2(1-z)}. A powder mixture of 2 mg NaCl and 10 mg of V₂O₅:MoO₃:WO₃ = 1:5:3 in the aluminium oxide boat was placed in the centre of the quartz tube. Another aluminium oxide boat containing S and Se powder was placed in the upstream. The furnace was heated with a ramp rate of 50 °C min⁻¹ to the growth temperature (760–840 °C) and held at this temperature for 10–20 min before cooling down to room temperature naturally. Ar/H₂ with a flow rate of 100/5 sccm was used as the carrier gas.

1 T' MoTe₂-2 H MoTe₂ in-plane heterostructures. A mixed powder of 4 mg NaCl and 14 mg MoO₃ in the aluminium oxide boat was placed in the centre of the quartz tube. The furnace was heated to a growth temperature of 720 °C with a ramp rate of 50 °C min⁻¹ and held for 3 min, and then quickly cooled to a growth temperature of 650 °C and held for 5 min and then cooled down to room temperature naturally. Ar/H₂ with flow rates of 80/20 sccm and 20/4 sccm was used as the carrier gas for 1 T' MoTe₂ and 2 H MoTe₂ growth, respectively.

MoS₂-NbSe₂ vertically stacked heterostructure. MoS₂ was synthesized first. A mixed powder of 0.5 mg NaCl and 3 mg MoO₃ in the aluminium oxide boat was placed in the centre of the tube. The furnace was heated to the growing temperature (600–800 °C) with a ramp rate of 50 °C min⁻¹. The growth time is 3 min. Ar (or Ar/H₂) with a flow rate of 80 sccm (or 80/5 sccm) was used as the carrier gas. The as-obtained MoS₂ was quickly transferred to another furnace for heterostructure growth. For the NbSe₂ growth, a mixed powder of 2 mg NaCl and 10 mg Nb₂O₅ and in the aluminium oxide boat was placed in the centre of the quartz tube. Another aluminium oxide boat containing Se powder was placed in the upstream. The furnace was heated with a ramp rate of 50 °C min⁻¹ to the growth temperature of 700 °C and held at this temperature for 10 min before cooling down to room temperature naturally. Ar/H₂ with a flow rate of 60/4 sccm was used as carrier gas.

We note that the weight ratio between salt and metal precursors can be tuned. Typically, for the synthesis of alloys, we fixed the weight ratio at 1:1 for the precursors. Taking Mo_{1-x}Re_xS₂ and WS_xTe_{2-x} as examples, by tuning the ratio between Mo and Re, and between S and Te, we can control the value of *x*.

STEM. STEM samples were prepared with a poly (methyl methacrylate) (PMMA)-assisted method or PMMA-free method with the assistance of an iso-propyl alcohol droplet. For some water-sensitive materials, we used a non-aqueous transfer method. STEM imaging and EELS analysis were performed on a JEOL 2100 F with a cold field-emission gun and an aberration corrector (the DELTA corrector) operating at 60 kV. A low-voltage modified Gatan GIF Quantum spectrometer was used for recording the EELS spectra. The inner and outer collection angles for the STEM image (β₁ and β₂) were 62 mrad and 129–140 mrad, respectively, with a convergence semi-angle of 35 mrad. The beam current was about 15 pA for the annular dark-field imaging and the EELS chemical analyses.

TG-DSC. TG-DSC measurements were performed using a Netzsch STA 449 C thermal analyser. Approximately 10 mg of the sample were loaded into an aluminium oxide crucible and heated at 10 K min⁻¹ from 20 °C to 920 °C. The 95 vol% Ar/5 vol% H₂ with a flow rate of 40 ml min⁻¹ was used as the carrier gas.

XPS. XPS measurements were performed using a monochromated Al Kα source (*hν* = 1486.6 eV) and a 128-channel mode detection Physical Electronics Inc. original detector. XPS spectra were acquired at a pass energy of 140 eV and a take-off angle of 45°.

Data availability. The main data supporting the findings of this study are available within the paper and its Supplementary Information. Extra data are available from the corresponding authors upon request.